

See discussions, stats, and author profiles for this publication at: <https://www.researchgate.net/publication/323449509>

Theoretical design and performance of $\text{In}_x\text{Ga}_{1-x}\text{N}$ single junction solar cell

Article in *Optik - International Journal for Light and Electron Optics* · February 2018

DOI: 10.1016/j.ijleo.2018.02.106

CITATIONS

28

READS

403

5 authors, including:



Y. Marouf

Université de Biskra

3 PUBLICATIONS 40 CITATIONS

[SEE PROFILE](#)



Lakhdar Dehimi

University of Batna 1

71 PUBLICATIONS 536 CITATIONS

[SEE PROFILE](#)



Fayçal Bouzid

Research Center In Industrial Technologies

18 PUBLICATIONS 128 CITATIONS

[SEE PROFILE](#)



Fortunato Pezzimenti

Mediterranean University of Reggio Calabria

65 PUBLICATIONS 692 CITATIONS

[SEE PROFILE](#)

Some of the authors of this publication are also working on these related projects:



Modelling and Simulation of 4H-SiC and GaN as temperature and UV detector [View project](#)



Low Breakdown Voltage 4H-SiC MOSFET for Photovoltaic Module-Level Applications [View project](#)

Theoretical design and performance of $\text{In}_x\text{Ga}_{1-x}\text{N}$ single junction solar cell

Y. Maarouf, L. Dehimi, F. Bouzid, F. Pezzimenti and F.G. Della Corte

Abstract: The insertion of optimized Window and BSF layers on an $\text{In}_x\text{Ga}_{1-x}\text{N}$ p-n basic single junction (BSJ) solar cell is the chief reason behind the reduction of front and back recombinations. In this context, this work is focused on the selection of the suitable parameters including the In content, thickness and doping concentration for the $\text{In}_x\text{Ga}_{1-x}\text{N}$ inserted layers, that gives the best photovoltaic performances. At this aim, numerical simulations were performed using the computational numerical modeling TCAD Silvaco® Atlas to design, optimize the $\text{In}_x\text{Ga}_{1-x}\text{N}$ BSJ and extract the above Window and BSF parameters that enhance the BSJ performances. A short circuit current density of $J_{sc} = 26.15 \text{ mA/cm}^2$, $V_{oc} = 0.904 \text{ V}$ and $FF = 79.67 \%$ are obtained under AM1.5G illumination, exhibiting a maximum conversion efficiency of ($\eta = 19.62 \%$). Other parameters like external quantum efficiency, electric field developed, the J-V curve and the power density curve are also calculated and plotted for the designed solar cell.

Key words: InGaN solar cell; Bsf layer; Window layer; Silvaco Atlas

1. Introduction

As the demand of energy and emphasis on environmental protection increase, solar energy is expected to become the major energy source [1]. Solar cells still remain the best way yet determined to harness energy from the sun, which is literally the unlimited source of renewable and clean energy [2]. To attain the expected breakthrough of photovoltaic technology as a competitive energy source against fossil fuels, the cell higher conversion efficiency, low cost and stability are the main factors [3]. Several materials were utilized to perform solar cells, the most common material used for the production of photovoltaic cells is silicon which is now approaching his theoretical maximum efficiency [4,5].

III-V group materials have been widely used for tandem solar cells for the space application, such as GaAs stacked with InGaP and Ge. The toxicity of arsenic in GaAs, the InGaP low resistance against irradiation damage and the indirect bandgap of the Ge are the biggest barriers of these materials [3]. InGaN is an alternative photovoltaic material, it has become a promising candidate for high-efficiency solar cells due to its attractive features. Among these, the following are of most interesting: first, the direct band gap lying from 0.7 eV (InN, in the near IR) to 3.4 eV (GaN, in the mid-UV), which can absorb the full solar spectrum by a single material InGaN with different indium contents [6]. In addition, InGaN alloys exhibit a much higher resistance to high-energy (2 MeV) photon irradiation than currently used PV materials such as GaAs and GaInP and, therefore, offer great potential for a radiation-hard high-efficiency solar cell for space applications. Furthermore, InGaN alloys have the advantages of high carrier mobility, high drift velocity,

high thermal conductivity, and high temperature resistance [7]. Finally, InGaN alloys display high absorption coefficients ($\sim 10^5 \text{ cm}^{-1}$) [8,9]. Thus, only a few hundred nanometers of InGaN material are required to absorb most of the incident light, thereby rendering moderately expensive indium more cost effective [5].

Abdoulwahab Adaine et al have numerically studied an InGaN p-n junction solar cell using the Atlas® device simulation software from the Silvaco® suite, an optimum efficiency of 17.8% was obtained [10].

In this paper, we conduct numerical simulations using same simulation environment to investigate the effect of the BSF and Window layers on the performance of InGaN-based solar cells and calculate the physical properties of the p-n junction such as the short circuit current density, open circuit voltage, fill factor and conversion efficiency by varying the indium content, device structures, doping densities of each layer.

2. Modeling and simulations

2.1 Software and device structure

The device structure as designed in this work, represented schematically in Fig.1, is an $\text{In}_x\text{Ga}_{1-x}\text{N}$ p-n BSJ solar cell, in which we have introduced two $\text{In}_x\text{Ga}_{1-x}\text{N}$ layers, one acting as a Back surface field (BSF) at the bottom and the other as a window at the top.

This device is simulated under AM1.5G spectrum and a temperature of 300 K by using the Atlas® device simulation software, a physically-based device simulator from the Silvaco® suite, in which we implemented our physical models. It predicts the electrical characteristics that are associated with specified physical structures and bias conditions. This is achieved by approximating the

operation of a device onto a two dimensional grid, consisting of a number of grid points called nodes. By applying a set of differential equations, derived from Maxwell's laws and solved by the Newton coupled and Gummel decoupled methods onto this grid, the transport of carriers (including the Poisson and continuity equations on electrons and holes) can be simulated through a structure [11].

Window	$(x_{Win} - d_{Win} - N_{Win})$	p⁺
Emitter	$(x - d_E - N_a)$	p
Base	$(x - d_B - N_d)$	n
Bsf	$(x_{Bsf} - d_{Bsf} - N_{Bsf})$	n⁺

Fig. 1. In_xGa_{1-x}N BSJ device structure. The parameter x represents the In concentration, d is the layer thickness, N is the doping concentration.

2.2 Physical modeling

Although the Poisson and continuity equations represent the fundamental laws governing the operation of a semiconductor device, additional models are often necessary to properly account for the dynamic nature of electrons and holes and to elaborate on the rich theory of device physics. These models supplement the Poisson and continuity equations by determining or modifying the variables contained in those laws. Among these:

2.2.1 Mobility model

The following expression, based upon the work of Caughey and Thomas [12,13] is used to model doping and temperature-dependent mobilities for electrons μ_n and holes μ_p .

$$\mu_m = \mu_{1m} \left(\frac{T}{300} \right)^{\alpha_m} + \frac{\mu_{2m} \left(\frac{T}{300} \right)^{\beta_m} - \mu_{1m} \left(\frac{T}{300} \right)^{\alpha_m}}{1 + \left(\frac{N}{N_m^{crit} \left(\frac{T}{300} \right)^{\gamma_m}} \right)^{\delta_m}} \quad (1)$$

where m is either n or p , N is the doping concentration in cm^{-3} , T is the absolute temperature in degrees Kelvin (K). N^{crit} , the n or p subscripted μ_1 , μ_2 and δ which are summarized in Table 1, are the model parameters which depend on the Indium composition. The n or p subscripted α , β and γ have been estimated to 1 [14,15].

Table 1. InN, GaN and In_xGa_{1-x}N material mobility parameters used in simulations [15, 16].

Parameter	GaN	InN
μ_{1n} ($cm^2 V^{-1} s^{-1}$)	295	1982.9
μ_{2n} ($cm^2 V^{-1} s^{-1}$)	1460	10885
δ_n	0.71	0.7439
N_n^{crit} ($\times 10^{16} cm^{-3}$)	7.7	10
μ_{1p} ($cm^2 V^{-1} s^{-1}$)	3.0	3.0
μ_{2p} ($cm^2 V^{-1} s^{-1}$)	170	340
δ_p	2.0	2.0
N_p^{crit} ($\times 10^{17} cm^{-3}$)	10	8.0

2.2.2 Recombination models

The Shockley-Read-Hall (SRH) expressed by equation (2) [17,18] is used to model the indirect recombination of charge carriers that occurs in the presence of traps (or defects) within the semiconductors bandgap.

$$R_{SRH} = \frac{np - n_i^2}{\tau_p (n + n_i e^{(ETRAP/kT)}) + \tau_n (p + n_i e^{(-ETRAP/kT)})} \quad (2)$$

where ETRAP is the difference between the trap energy level and the intrinsic Fermi level $ETRAP = E_t - E_i$, T is the absolute temperature in degrees Kelvin, τ_n and τ_p are the electron and hole lifetimes. This model only presumes one trap level which is $ETRAP=0$ and it corresponds to the most efficient recombination centre.

The second indirect recombination model we took into consideration is the Auger recombination, described by the expression (3) [19]. It occurs through a three particle transition whereby a mobile carrier is either captured or emitted.

$$R_{Auger} = C_{Augn}(pn^2 - nn_i^2) + C_{Augp}(np^2 - pn_i^2) \quad (3)$$

The radiative (optical) recombination model due to the direct bandgap transition is also taken into account and it is modeled as follows (4) [13]:

$$R_{rad} = C_{opt}(np - n_i^2) \quad (4)$$

The minority carrier lifetime τ_n and τ_p , the Auger and the radiative coefficients (C_{Augn} , C_{Augp} and C_{opt}) are taken equal to 1 ns, $1.4 \times 10^{-30} cm^6/s$ and $2.4 \times 10^{-11} cm^3/s$ respectively [15,16,20].

2.2.3 Optical model

In Atlas[®], the complex index of refraction with its real (the refractive index n) and imaginary (extinction coefficient k) parts of the various material regions in the structure must be specified. For many of the more common semiconductors, there are built-in tables of index versus wavelength that do not include the $\text{In}_x\text{Ga}_{1-x}\text{N}$ ternary alloys. To overcome this problem we used the absorption coefficient model proposed previously [15].

$$\alpha \text{ (cm}^{-1}\text{)} = 10^5 \times \sqrt{C(E_{ph} - E_g) + D(E_{ph} - E_g)^2} \quad (5)$$

To express the $\text{In}_x\text{Ga}_{1-x}\text{N}$ real part of the complex refractive index, we used the Adachi's refractive index model [11] given by Equation 6.

$$n(E_{ph}) = \sqrt{\frac{A}{(E_{ph}/E_g)^2} \left[2 - \sqrt{1 + \frac{E_{ph}}{E_g}} - \sqrt{1 - \frac{E_{ph}}{E_g}} \right] + B} \quad (6)$$

where E_{ph} is the incoming photon energy, E_g is material bandgap at a given Indium composition x . The compositional dependence of the C and D parameters are given by the expressions in Equations 7 and 8, their empirical values are listed in Table 2. Parameters A and B are linearly interpolated (Equations 9 and 10) from those of the binary material which were experimentally measured ($A^{\text{InN}} = 13.55$ and $B^{\text{InN}} = 2.05$) for InN and ($A^{\text{GaN}} = 9.31$ and $B^{\text{GaN}} = 3.03$) for GaN [16,21].

$$C = 3.525 - 18.29x + 40.22x^2 - 37.52x^3 + 12.77x^4 \quad (7)$$

$$D = -0.6651 + 3.616x - 2.460x^2 \quad (8)$$

$$A = 13.55x + 9.31(1 - x) \quad (9)$$

$$B = 2.05x + 3.03(1 - x) \quad (10)$$

Table 2. C and D empirical parameters values used to calculate the $\text{In}_x\text{Ga}_{1-x}\text{N}$ absorption coefficient [8,22].

Indium composition	C (eV ⁻¹)	D (eV ⁻²)
1	0.69642	0.46055
0.83	0.66796	0.68886
0.69	0.58108	0.66902
0.57	0.60946	0.62182
0.5	0.51672	0.46836
0	3.52517	-0.65710

A Matlab code has been developed in the aim to implement optical properties in Atlas[®]. It calculates the refractive index, converts the absorption coefficient into extinction coefficient using the above equations and creates a text file that contains ordered triplets of wavelength, refractive index, and extinction coefficient.

2.2.4 Material parameters

The bandgap (E_g), relative permittivity (ϵ), electron affinity (χ), effective density of states in the conduction and the valence band (N_C and N_V), electron and hole effective mass (m_e and m_h) are summarized in Table 3.

Table 3. InN, GaN, $\text{In}_x\text{Ga}_{1-x}\text{N}$ material parameters used in simulations

Parameter	GaN	InN	$\text{In}_x\text{Ga}_{1-x}\text{N}$
E_g (eV) at 300 K [22]	3.42	0.7	$0.7x + 3.42(1 - x) - 1.43x(1 - x)$
ϵ [23]	8.9	15.3	$15.3x + 8.9(1 - x)$
χ (eV) [23]	4.1	5.6	$4.1 + 0.7(3.4 - E_g)$
N_C ($\times 10^{17} \text{ cm}^{-3}$) [23]	23	9.1	$9.1x + 23(1 - x)$
N_V ($\times 10^{19} \text{ cm}^{-3}$) [3]	4.6	5.3	$5.3x + 4.6(1 - x)$
m_e [21]	0.2	0.12	$0.12x + 0.2(1 - x)$
m_h [21]	1.0	0.17	$0.17x + 1.0(1 - x)$

3. Simulations results and discussion

Numerical simulations have been carried out for choosing the best structure parameters, such as indium composition, layers thicknesses and doping concentrations, which lead to an optimal performance of the $\text{In}_x\text{Ga}_{1-x}\text{N}$ single solar cell. BSJ parameters were determined first, thereafter the BSJ performance was enhanced by inserting a Bsf and window layers and their parameters have been calculated. The J-V solar cell characteristics (including short-circuit current density J_{sc} and open-circuit voltage V_{oc} parameters), the efficiency η , the external quantum efficiency EQE , electric field and the power density curve are extracted and also plotted using TonyPlot Silvaco[®] Software, the interactive graphics and analysis package.

3.1 BSJ solar cell performance

The effect of the indium composition on the performance of the $\text{In}_x\text{Ga}_{1-x}\text{N}$ p-n BSJ solar cell is shown in Fig.2. (Which is the total irradiation ? 1 kW/m² ?) It is clearly seen that the efficiency η first increases with the increase of indium composition (due to the decrease in the bandgap), reaches a maximum value (at $x = 56\%$) in the range of 50% to 60% that coincides with the bandgap of 1.45 eV to 1.70eV, corresponding to the visible wavelengths which cover the most part of the AM1.5

spectrum and then decreases with the increase of indium composition.

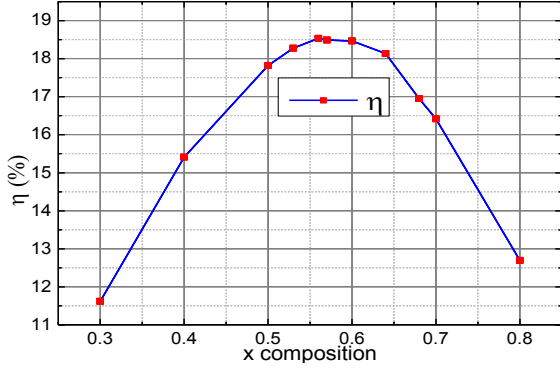


Fig. 2. Conversion efficiency of the $\text{In}_x\text{Ga}_{1-x}\text{N}$ PN solar cell as a function of indium composition. Specify the other parameters of fig. 1 used for the simulation of this efficiency.

Fig.3 displays the short-circuit current density (J_{sc}), the open-circuit voltage (V_{oc}), and the conversion efficiency (η) as a function of the acceptor doping concentration N_a with various thickness d_E of the emitter.

On the one hand, the short-circuit current density (J_{sc}) (Fig.3.a) increases with the decrease of the emitter thickness d_E and reaches a maximum for $d_E = 10 \text{ nm}$. What happens for $d_E < 10 \text{ nm}$? Maybe it increases even more.

The effect of the thinner emitter is to mask the effect of surface recombination by reducing distance between the surface and the space charge region and enhance the photogeneration resulting from the increase in external quantum efficiency EQE with the decreasing emitter thickness d_E as shown in Fig.4, this means that as the emitter becomes thinner and thinner, a larger amount of photons throughout the spectrum (from the near bandgap wavelength $\sim 0.8 \text{ nm}$ to the shorter wavelengths) are able to reach the base.

On the other hand, with 10 nm emitter thickness, J_{sc} increases first, reaches a maximum and then decreases as the acceptor doping concentration N_a increases. From equation (1), we could see that the carrier mobility μ decreases for high acceptor doping concentration ($N_a > 1 \times 10^{18} \text{ cm}^{-3}$), this implies a decrease in both minority carrier diffusivity D and minority carrier diffusion length L known by the relations (11, 12) and so on a decrease in J_{sc} .

$$D = \left(\frac{K_B T}{q} \right) \mu \quad (11)$$

$$L = \sqrt{D \tau} \quad (12)$$

Where τ is the minority carrier life time, K_B is the Boltzmann's constant, q is the absolute electric charge of electron and T is the Kelvin temperature.

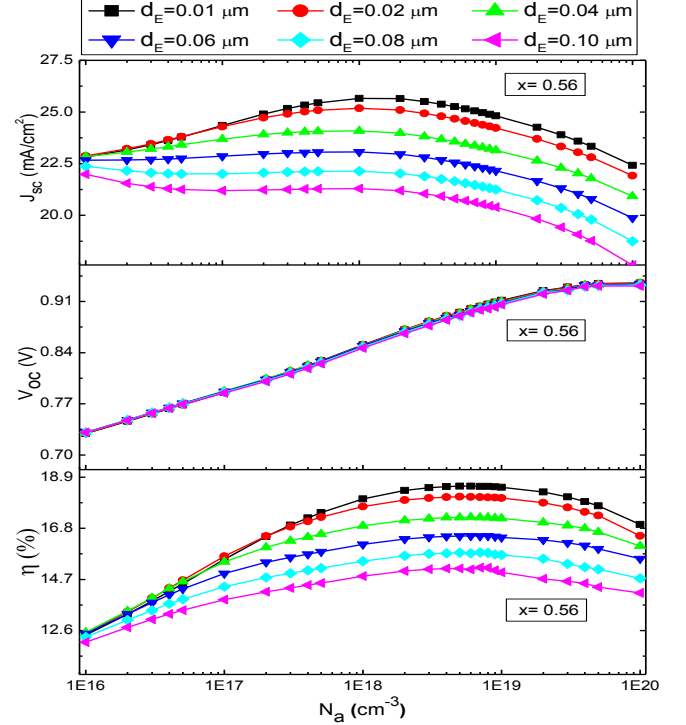


Fig. 3. (a) Short circuit current density J_{sc} , (b) open circuit voltage V_{oc} , (c) conversion efficiency η as function of the acceptor concentration N_a with various emitter thickness d_E . What are the values of the other parameters of fig. 1 for these simulations? e.g. d_B , N_d , N_{Bsf} , What happens for $d_E < 10 \text{ nm}$?

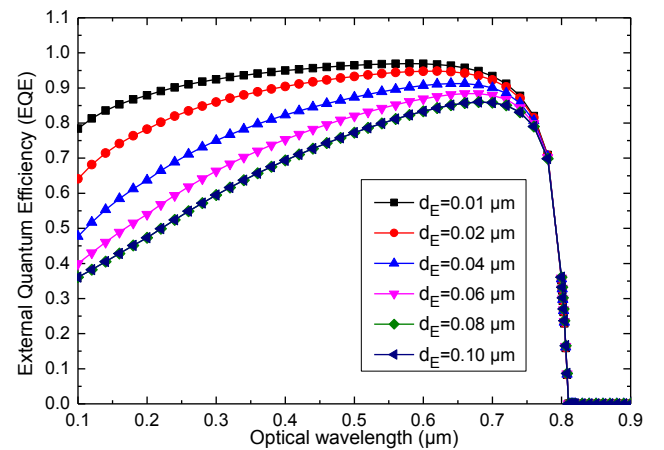


Fig.4. $\text{In}_{0.56}\text{Ga}_{0.44}\text{N}$ BSI solar cell External Quantum Efficiency (EQE) with various Emitter thickness d_E .

It can be seen from Fig.3.b and proved by the equations (13, 14), that the open-circuit voltage V_{oc} increases with the acceptor doping concentration N_a .

$$V_{oc} = \frac{K_B T}{q} \ln \left(\frac{J_{sc}}{J_0} + 1 \right) \quad (13)$$

$$J_0 = q n_i^2 \ln \left(\frac{D_n}{L_n N_a} + \frac{D_p}{L_p N_d} \right) \quad (14)$$

Where N_d is the donor doping concentration, J_0 is the saturation current density.

According to the previous study ($J_{sc} = f(d_E)$) and taking into account the equation (14), we conclude that the decrease in the thickness of d_E causes an increase in both the photocurrent J_{sc} and the saturation current J_0 , which leads to an insignificant variation of the open circuit voltage V_{oc} as a function of d_E (eq. 13)

The conversion efficiency η represents the combined effects of J_{sc} and V_{oc} . On the one hand η increases as the acceptor doping concentration N_a increases due to the increase in both J_{sc} and V_{oc} , reaches a peak value at $N_a = 5 \times 10^{18} \text{ cm}^{-3}$ then decreases for further increase of N_a , this decrease is mainly results from the decrease in J_{sc} . On the other hand η increases with the decrease of the emitter thickness d_E , a maximum conversion efficiency of about 18,53 (%) is achieved for a 10 nm emitter thickness.

In order to study the influence of the base on the efficiency, the thickness and the doping concentration of the emitter were set to 10 nm and $5 \times 10^{18} \text{ cm}^{-3}$ respectively. In this context, thickness d_B and doping concentration N_d of the base were varied in intervals $[0.1 - 2] \mu\text{m}$ and $[1 \times 10^{15} - 1 \times 10^{17}] \text{ cm}^{-3}$ respectively, the results obtained are reported in Fig.5. We note that the conversion efficiency η attains a maximum for $N_d = 5 \times 10^{15} \text{ cm}^{-3}$, decreases with the increased base doping concentration, increases with the increased base thickness and saturates for $d_B = 1 \mu\text{m}$, a sufficient thickness that can exploit a wide range of the solar spectrum.

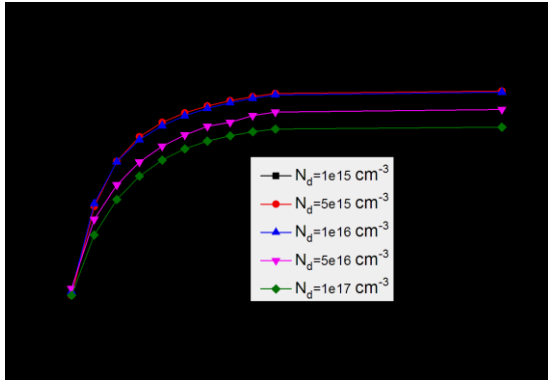


Fig.5. The efficiency η as a function of base thickness d_B with various doping concentration N_d .

3.2 Bsf layer effect

To improve the performance of the device structure, additional layers such as back surface field BSF, window (also known as front surface field FSF) are added to the BSJ solar cell by increasing the doping in the semiconductor near the surfaces, creating two other junctions p^+-p and $n-n^+$ at the top and the bottom of the cell. Fig.6 illustrates the device efficiency η as a function of the BSF thickness d_{BSf} with various doping concentration N_{BSf} and different Indium content x_{BSf} . From the figure, a maximum value of 19.30 % efficiency was found for $d_{BSf} = 50 \text{ nm}$, $N_{BSf} = 5 \times 10^{19} \text{ cm}^{-3}$ and $x_{BSf} = 56 \%$.

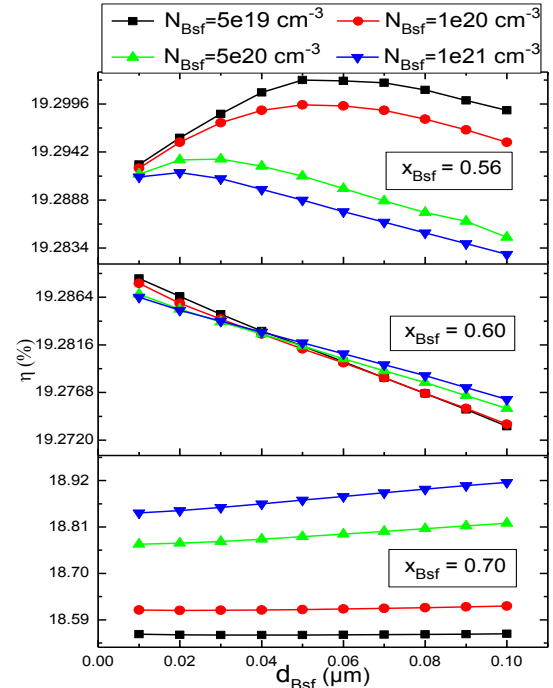


Fig.6. The Efficiency η as a function of BSF thickness d_{BSf} and doping concentration N_{BSf} .

The BSF layer generates an electric field across the $n-n^+$ junction that repel minority carriers from the surface towards the junction and prevent them from recombining at the surface. This electric field gets a maximum for 56 % of indium content and decreases with the increase of x_{BSf} as it is shown in the cutline view of Fig.7.

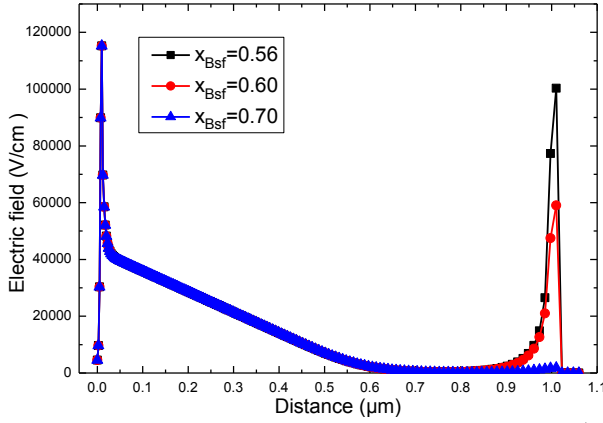


Fig.7. Cutline view of electric field developed across n-n⁺ junction.

The short circuit current density J_{sc} , the open circuit voltage V_{oc} as a function of the BSF thickness d_{BSf} and the doping concentration N_{BSf} are plotted in Fig.8; their values corresponding to the best efficiency mentioned above are 25.784 (mA/cm^2) and 0.900 V respectively.

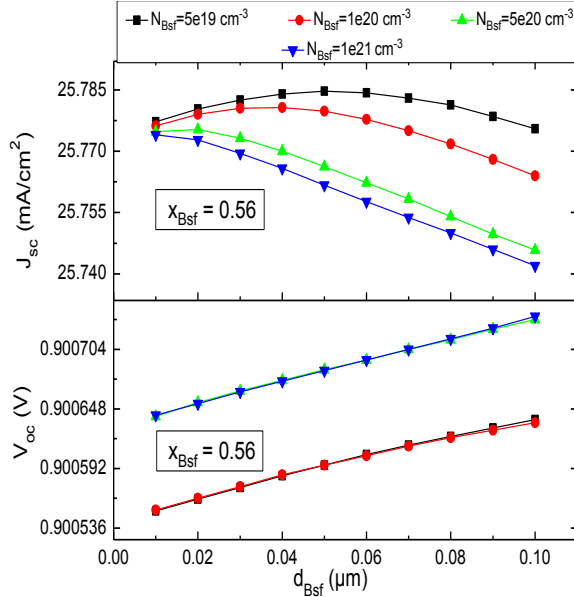


Fig.8. Short circuit current density J_{sc} and open circuit voltage V_{oc} as a function of d_{BSf} with various doping concentration N_{BSf} for $x_{BSf}=0.56$.

3.3 Window layer effect

The effect of the $\text{In}_x\text{Ga}_{1-x}\text{N}$ window layer was studied by varying its thickness d_{win} and doping concentration N_{win} for adjusted value of indium content x_{win} . Figs.9 and 10 show the variations of solar cell parameters versus window thickness and doping concentration.

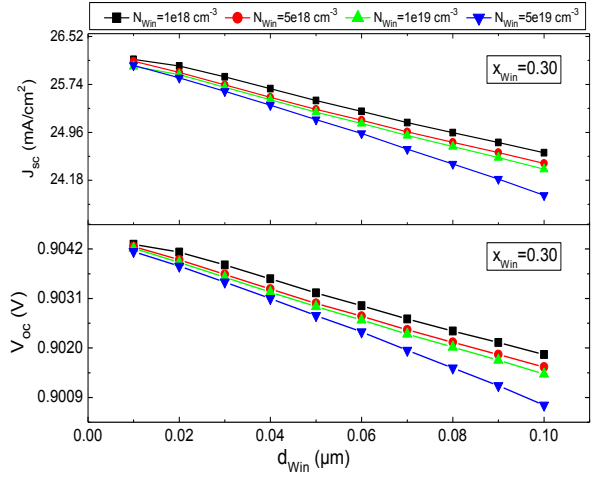


Fig.9. Short circuit current density J_{sc} and open circuit voltage V_{oc} as a function of window thickness d_{win} and doping concentration N_{win} for $x_{win}=30\%$.

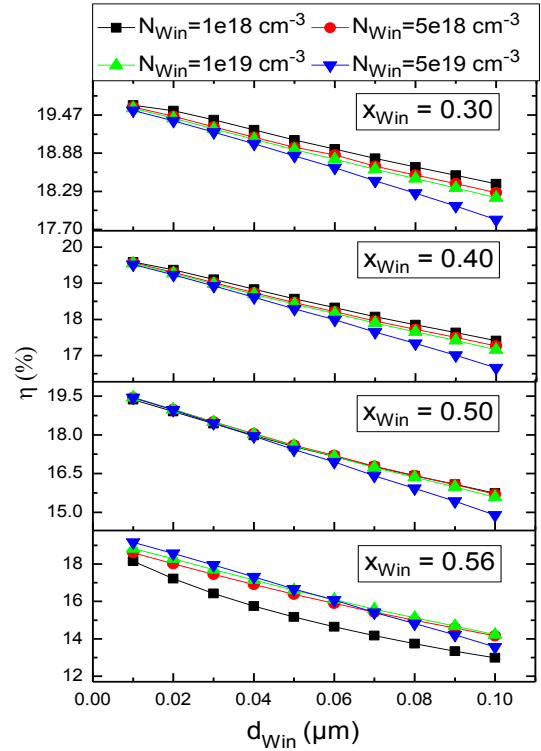


Fig.10. The Efficiency η as a function of window thickness d_{win} and doping concentration N_{win} with various indium content x_{win} .

From these figures it is clear that, our device shows maximum efficiency ($\eta = 19.62\%$) along with highest short circuit current ($J_{sc} = 26.15 \text{ mA}/\text{cm}^2$) and open circuit voltage $V_{oc} = 0.904 \text{ V}$ for an indium content, a window thickness and doping concentration of 30 %, 10 nm and $1 \times 10^{18} \text{ cm}^{-3}$ respectively. **What happens for $d_{win} < 10 \text{ nm}$ and $x_{win} < 30\%$?**

This can be explained by the fact that low indium content $x_{win} = 30\%$ (high bandgap) first, exhibits a

higher EQE leading to high photogeneration, second creates a highest electric field across the p^+-p junction that reflect and accelerate minority carriers towards the pn junction thus reducing surface recombination effects and increasing efficiency, compared to the other ratio of Indium 40, 50, 56 %, as it can be seen in the Figs.11 and 12.

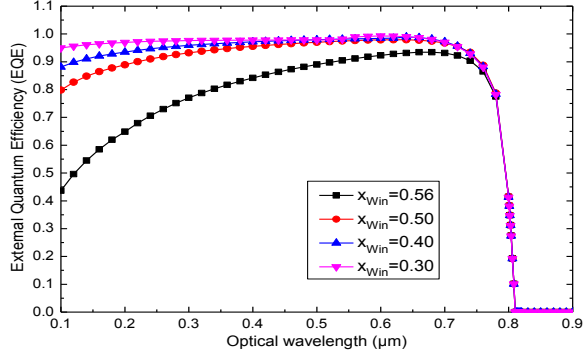


Fig.11. External Quantum Efficiency (EQE) with various indium content x_{Win} of window layer.

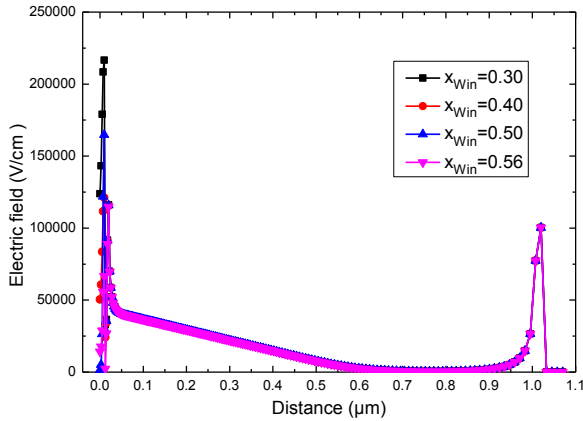


Fig.12. Cutline view of electric field developed across p^+-p junction

4. Conclusion

In this work, an $In_xGa_{1-x}N$ p-n BSJ homojunction solar cell was, initially, performed by changing In content, thickness and doping concentration of the emitter and the base, using the Silvaco® Atlas simulation software. For the optimized cell with a $0.01\mu m$ emitter thickness, $1\mu m$ base thickness, an acceptor concentration of $5 \times 10^{18}cm^{-3}$, a donor concentration of $5 \times 10^{15}cm^{-3}$ and an indium content of 56%, an optimal conversion efficiency, a short circuit current, an open circuit voltage and a fill factor of 18.53% (corresponding to a maximum power density of $17.79 mW/cm^2$), $25.26 mA/cm^2$, $0.895V$ and 78.68% were respectively obtained, as shown in the JV characteristic (Fig.13) and power density curve generated (Fig.14), these results are comparable favorably with those of the single junction in [10]. An improvement of the conversion efficiency has been observed by adding an

$In_xGa_{1-x}N$ Bsf and a wide bandgap window layers to the above optimized cell, it was removed up to 19.62% (corresponding to a maximum power density of $18.84 mW/cm^2$), with an In content of 56% and 30%, a thickness of $0.05\mu m$ and $0.01\mu m$, a doping concentration of $5 \times 10^{19}cm^{-3}$ and $1 \times 10^{18}cm^{-3}$ for the Bsf and window respectively.

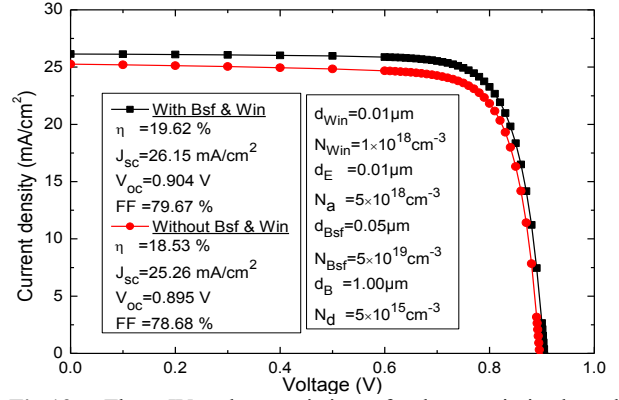


Fig.13. The JV characteristic of the optimized cell.

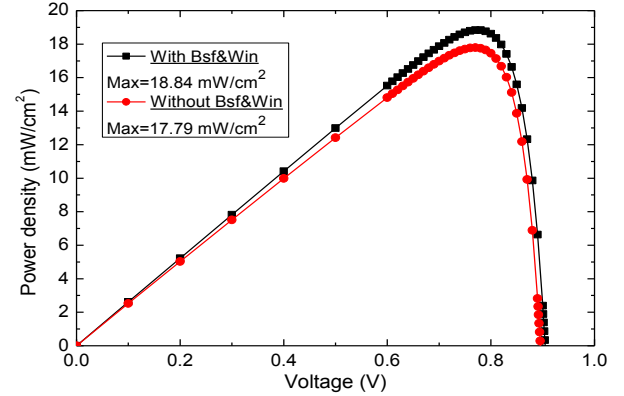


Fig.14. The power density curve of the optimized cell.

References many references are missing of details (journal, issue, year, pages, ...)

- [01] Ming-Han Hsieh and Yuh-Renn Wu. (2011). Numerical Modeling of $In_xGa_{1-x}N$ Silicon Multi-Junction Tandem Solar. *IEEE* , 002052. ??????
- [02] N. Akter, M. A. Matin, and N. Amin. (2013). High Performance $In_xGa_{1-x}N$ Tandem Solar Cells Designed from Numerical Analysis. *IEEE* , 469. ?????
- [03] N. Akter. (2014). DESIGN AND SIMULATION OF INDIUM GALLIUM NITRIDE MULTI-JUNCTION TANDEM SOLAR CELLS. *IJRET* , 315. ??????
- [04] K. Ameur, Z. Benamara, H. Mazari, N. Benseddik, R. Khelifi, M. Mostefaoui, N. Benyahya. (2014). Numerical simulation of solar cells based on III-V nitride compounds. *Opt Quant Electron* 46 , 194.
- [05] Chloe A.M. Fabien, W. Alan Doolittle. (2014). Guidelines and limitations for the design of high-efficiency $InGaN$ single-junction solar cells. *Solar Energy Materials & Solar Cells* 130 , 354.

-
- [06] S. Nacer, A. Aissat. (2015). Simulation and optimization of current matching multi-junction InGaN solar cells. *Opt Quant Electron* 47 , 3864.
- [07] Bhuiyan A G, Sugita K, Hashimoto A and Yamamoto A. (2012). InGaN Solar Cells: Present State of the Art and Important Challenges. *IEEE JOURNAL OF PHOTOVOLTAICS*, VOL. 2, NO. 3 , 276,277.
- [08] J.F. Muth, A.J.H. Lee, I.K. Shmagin, R.M. Kolbas, H.C. Caser., B.P. Keller, U.K. Mishra, S.P. DenBaars. (1997). Absorption coefficient, energy gap, exciton binding energy, and recombination lifetime of GaN obtained from transmission measurements. *Appl. Phys. Lett.* 71 , 2572–2574.
- [09] R. Singh, D. Doppalapudi, T.D. Moustakas, L.T. Romano. (1997). Phase separation in InGaN thick films and formation of InGaN/GaN double heterostructures in the entire alloy composition. *Appl. Phys. Lett.* 70 , 1089–1091.
- [10] A. Adaine, S. Hamady and N. Fressengeas. ((2016)). Simulation study of new InGaN p-layer free schottky based solar cell. *Superlattices and Microstructures* 96 , 121–133.
- [11] SILVACO Data Systems. (2013). Silvaco ATLAS User's Manual.
- [12] D.M. Caughey, R.E. Thomas. (1967). Carrier Mobilities in Silicon Empirically Related to Doping and Field. *Proc. IEEE* 55 , 2192–2193.
- [13] Schwierz, F. (2005). An electron mobility model for wurtzite GaN. *Solid-state electronics* 49 (6) , 889–895.
- [14] Xiaobin Zhang, Xiaoliang Wang, Hongling Xiao, Cuibai Yang, Junxue Ran, Cuimei Wang, Qifeng Hou and Jinmin Li. (2007). Simulation of In_{0.65}Ga_{0.35}N single-junction solar cell. *J. Phys. D: Appl. Phys.* 40 , 7335–7338.
- [15] G. Brown, J. Ager III, W. Walukiewicz, J. Wu. (2010). Finite element simulations of compositionally graded InGaN solar cells. *Solar Energy Materials and Solar Cells* 94 (3) , 478–483.
- [16] Y.C. Shen, G.O. Mueller, S. Watanabe, N.F. Gardner, A. Munkholm, M.R. Krames. (2007). Auger recombination in InGaN measured by photoluminescence. *Appl. Phys. Lett.* 91 , 141101.
- [17] SHOCKLEY.W, READ.W.T, “Statistics of the recombinations of holes and electrons”. Physical SHOCKLEY.W, READ.W.T, “Statistics of the recombinations of holes and electrons”. *Physical Review*, 1952, vol. 87, no5, p. 835–842. (n.d.).
- [18] HALL. R.N., “Electron Hole Recombination in Germanium”, *Physical Review*, 1952, vol. 87, no2, p.387. (n.d.).
- [19] DZIEWIOR J and W. SCHMID, Auger coefficient for highly doped and highly excited silicon, *Appl Phys Lett*, 1977, Vol 31, p 346–348. (n.d.).
- [20] Jani. O. K. (2008). Development of wide-band gap InGaN solar cells for high-efficiency photovoltaics. *PhD Thesis Georgia Institute of Technology August* .
- [21] M. Nawaz, A. Ahmad. (2012). A TCAD-based modeling of GaN/InGaN/Si solar cells. *Semiconductor Science and Technology* 27 (3) , 035019.
- [22] J. Wu, W. Walukiewicz, K.M. Yu, J.W. Ager III, E.E. Haller, H. Lu, W.J. Schaff. (2002). Small band gap bowing in In_xGa_{1-x}N alloys. *Appl. Phys. Lett.* 80 , 4741–4743.
- [23] Levinshtein M E, Rumyantsev S L and Shur M S. (2001). Properties of Advanced Semiconductor Materials. *Chichester, UK: Wiley* , pp 1–90.